https://doi.org/10.5194/egusphere-2025-5512
Preprint. Discussion started: 6 February 2026

DReaMIT: A Dynamical Reanalysis Framework for Modelling Surface-Based Temperature Inversions in Cold Environments

Victor Pozsgay[1], Nick Noad[2], Philip Bonnaventure[2], and Stephan Gruber[1]

[1]Department of Geography and Environmental Studies, Carleton University, Ottawa, Canada
[2]Department of Geography and Environment, University of Lethbridge, Lethbridge, Alberta, Canada

Correspondence: Victor Pozsgay (victor.pozsgay@carleton.ca)

Abstract. Surface-based temperature inversions (SBIs) are critical to high-latitude mountain climatology, shaping permafrost stability and near-surface thermal regimes. This study develops and evaluates a new surface-based inversion model, DReaMIT (Dynamical Reanalysis Model for Inversions of Temperature), that extends the framework of (Pozsgay and Gruber, 2025) by spatializing the inversion strength parameter (α) using hypsometric position rather than absolute elevation. The reformulated approach enables a unified calibration across two contrasting Yukon valleys (WS01 and WS02), improving model transferability and reducing site-specific bias. Exponentiation of the elevation variable captures the observed nonlinear decay of lapse rates within SBIs, consistent with in-valley observations where temperature increases of up to $8\,^{\circ}\mathrm{C}$ over $19\,\mathrm{m}$ were recorded. Model performance was assessed across the Yukon and Northwest Territories, where it successfully reproduced inversion structure even in areas with weaker or transient SBIs, such as Whitehorse and Haines Junction. Limitations were observed in flat regions with minimal hypsometric relief (e.g., Tulita, Old Crow), highlighting cases where microtopographic indices may better represent cold-air pooling potential. The new hypsometric formulation enhances the physical realism and spatial applicability of SBI modelling, providing an empirically-constrained, transferable tool for predicting near-surface temperature regimes and assessing permafrost sensitivity under northern climate change.

1 Introduction

Observational climate data are sparse and discontinuous in high-latitude (Urban et al., 2013; Way and Bonnaventure, 2015) and alpine regions (Oyler et al., 2015; Pepin et al., 2022). In contrast, climate reanalysis products provide spatially- and temporally-consistent datasets that extend back more than 75 years, since 1940 for ERA5 (Hersbach et al., 2020) and 1948 for JRA-3Q (Hersbach et al., 2020; Kosaka et al., 2024). These datasets are improving through updates to their modelling and forecasting systems, resulting in comprehensive coverage of surface and atmospheric conditions at multiple pressure levels. Consequently, reanalysis products are a valuable resource in areas that have sparse observational data and are used to inform modelling, such as predictions of permafrost (e.g., Liu et al., 2025; Obu et al., 2019; Tao et al., 2019; Fiddes et al., 2015) and hydrological (e.g., Nkiaka et al., 2017; Tarek et al., 2020).

However, the coarse spatial resolution of reanalysis products (tens of kilometers) limits their applicability in mountainous terrain, where complex topography can produce climate variations comparable to those observed across thousands of kilometers

https://doi.org/10.5194/egusphere-2025-5512
Preprint. Discussion started: 6 February 2026

in latitude (Riseborough et al., 2008). This sub-grid heterogeneity, and the local processes it drives, are not captured by coarse resolution (Etzelmüller, 2013).

To address this limitation, a variety of downscaling methods have been developed to scale coarse resolution climate reanalysis data to finer resolutions or scale-free point locations (e.g., Draeger et al., 2024; Ntagkounakis et al., 2023; Wang et al., 2016; Zhang et al., 2020). Among these, TopoSCALE (Fiddes and Gruber, 2014) and TopoCLIM (Fiddes et al., 2022) use topography-based parameterizations to reproduce small-scale variability, while Globsim (Cao et al., 2019) extends these methods by integrating multiple reanalysis datasets to generate meteorological time series for specific sites. These models have been shown to effectively predict weather conditions with limited bias; however, residual errors remain in regions where complex local processes are not resolved in the reanalysis model (Daly et al., 2008; Roberts et al., 2019). Furthermore, reanalysis data can have regional or temporal trends in bias, especially given that they are less reliable for earlier periods (Urraca and Gobron, 2023).

To reduce these biases, Pozsgay and Gruber (2025) developed a model that explicitly accounts for the influence of surface-based temperature inversions (SBIs) on near-surface air temperature and that includes a temporal bias correction parameter. This model dynamically corrects downscaled reanalysis data at hourly time steps. This is done by incorporating a conceptual framework introduced by Noad et al. (2023), which defines SBI magnitude as the strength of an SBI (temperature increase from the bottom to the top of the SBI) added to the expected surface air temperature if the lapse rate above the SBI layer were to continue to the surface.

This approach addresses a key limitation in downscaling methods, an assumption that the lapse rates are normal below reanalysis grid elevation, disregarding intense SBIs at these low elevations. In subarctic valleys, prolonged periods of nocturnal radiative cooling during the winter promote deep, intense, and long-lasting SBI events (Fochesatto et al., 2015; Mayfield and Fochesatto, 2013; Noad and Bonnaventure, 2022, 2024). These SBIs generate strongly positive mean annual lapse rates (upwards to $25\,^{\circ}\mathrm{C\,km^{-1}}$) within the first 100 to 150 m above the valley floor (Noad and Bonnaventure, 2025), leading to substantial biases when unresolved below the grid level of the reanalysis product.

Initial testing of the Pozsgay and Gruber (2025) model using a dense network of air temperature sensors across two subarctic valleys demonstrated that the model performs well when calibrated locally (Noad et al., 2025), but suffers from a lack of transferability. In this study, we aim to enhance the generalizability of the Pozsgay and Gruber (2025) inversion correction model by testing new parameters beyond the original use of absolute elevation. Specifically, we evaluate additional topographic variables (e.g., relative elevation and hypsometry) to better represent the influence of local terrain on cold-air pooling and SBI dynamics. By calibrating these parameters across multiple valleys and testing them at other locations in northwestern Canada, we will identify the optimal parameters and functional form of the model to increase prediction performance regionally, without requiring additional local calibration. This work contributes to the improved use of reanalysis in their ability to represent sub-grid processes in complex terrain. The resulting model parameterization will increase their reliability for important applications such as permafrost or hydrological modelling.

https://doi.org/10.5194/egusphere-2025-5512
Preprint. Discussion started: 6 February 2026

2 Study area

2.1 Dempster

The study area of this paper consists of two northcentral Yukon valleys, approximately 120 km to the north-east of Dawson City, around Distincta Peak (1790 m a.s.l.), the dominant point in the subrange of mountains. These valleys will be referred to as WS01 and WS02 (for weather station 1 and 2), and correspond to valleys labelled as SVWS and NVWS, respectively, in Noad and Bonnaventure (2022). Those sites are easily accessible by road, being located in the immediate vicinity of the Dempster Highway. They were shown to be prone to intense, frequent, and long-lasting inversion events (Noad and Bonnaventure, 2022, 2025).

The two valley floors are separated by approximately 8 km, with WS01 to the south of Distincta Peak, and WS02 to the north. The former is an approximately 5.5 km-long V-shaped valley, with elevations ranging from 950 m at the outlet and 1700 m on the closest highest ridge. The latter is an approximately 6.5 km-long U-shaped valley, with elevations comprised between 1040 and 1790 m. The valleys' outlet is oriented towards the southeast for WS01, and to the north for WS02.

The network of air temperature loggers consists of 24 locations in valley WS01, and 26 in WS02. The locations are chosen to sample the widest range of elevation, slope, aspect angle, and degree of valleyness (Cao et al., 2017).

2.2 Dawson

The model calibration of this paper will be tested on the dataset presented in Pozsgay and Gruber (2025), where five weather stations are distributed within a 25 km radius from the Dawson airport, and with elevations ranging from 370 to 1200 m.

2.3 ECCC/NAVCAN weather stations

Finally, the temperature inversion model will also be applied to various sites across northern Canada, in the Yukon and Northwest Territories. We selected 13 ECCC/NAVCAN weather stations (Fig. 1, see Table E1 for coordinates) because they span a wide spatial area and a variety of topographic conditions, from river delta to mountainous terrain.

Then, we report the distribution of elevations in a radius of 50 km around each station in Fig. 2, together with all sites from the Dempster and Dawson areas.

3 Methods

3.1 In-situ observations

The 50 locations scattered across the two valleys of the study area are instrumented with passively-ventilated air temperature loggers. Air temperature data was retrieved at the end of the 2024 summer during fieldwork.

Observational data for the Dawson area is taken from (Pozsgay and Gruber, 2025), and was originally provided by the Yukon Geological Survey. Finally, the air temperature data for the Dawson airport and for the 10 locations described in Table E1 is

https://doi.org/10.5194/egusphere-2025-5512
Preprint. Discussion started: 6 February 2026

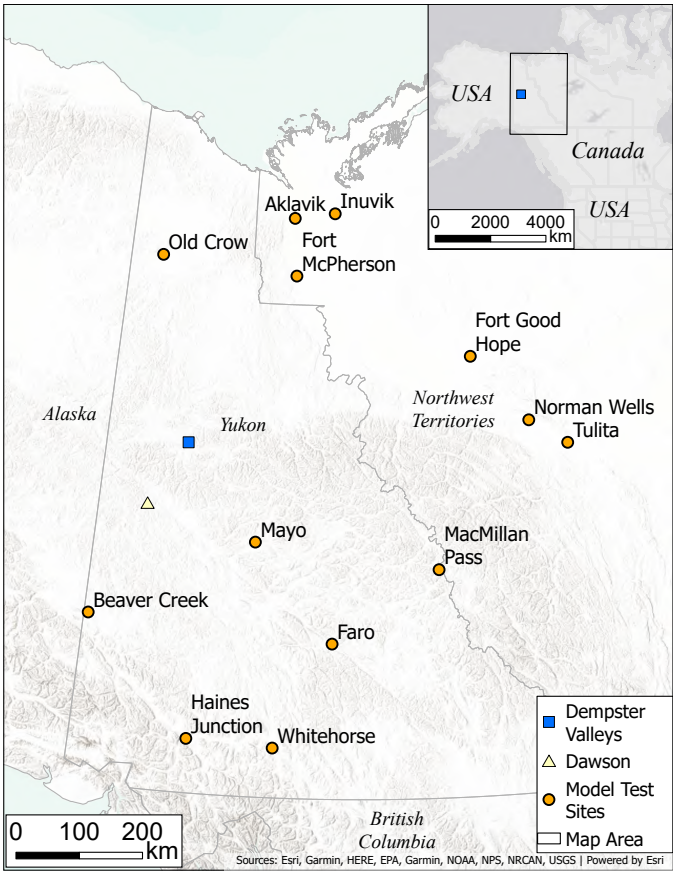

Figure 1. The Dempster study valleys (blue point), Dawson City (yellow point), and 13 Environment Climate Change Canada (ECCC) and Navigation Canada (NAVCAN) weather station locations (orange points) situated across Yukon and Northwest Territories.

managed by Environment and Climate Change Canada (ECCC) and is downloaded with the R-package weathercan (LaZerte and Albers, 2018).

3.2 Reanalysis data

Reanalysis data products are accessible globally for several decades. They are consistent and gapless in both time and space, allowing researchers to study uninstrumented areas or to provide additional data where observations might be available. In this study, we use hourly ERA5 data from the European Centre for Medium-Range Weather Forecasts (ECMWF) (Hersbach et al., 2023a, b) since 1940 and 6-hourly JRA-3Q data from the Japan Meteorological Agency (JMA) (Kosaka et al., 2024) (downscaled hourly) since since 1947. The former is available on a regular $0.25° \times 0.25°$ grid in latitude and longitude, while the latter uses a TL479 Gaussian grid instead with a spatial resolution of $0.375° \times 0.375°$. We download data divided into three categories: constant (geopotential, land-sea mask), single level ($2\,\mathrm{m}$ temperature), and pressure levels (air temperature).

https://doi.org/10.5194/egusphere-2025-5512
Preprint. Discussion started: 6 February 2026

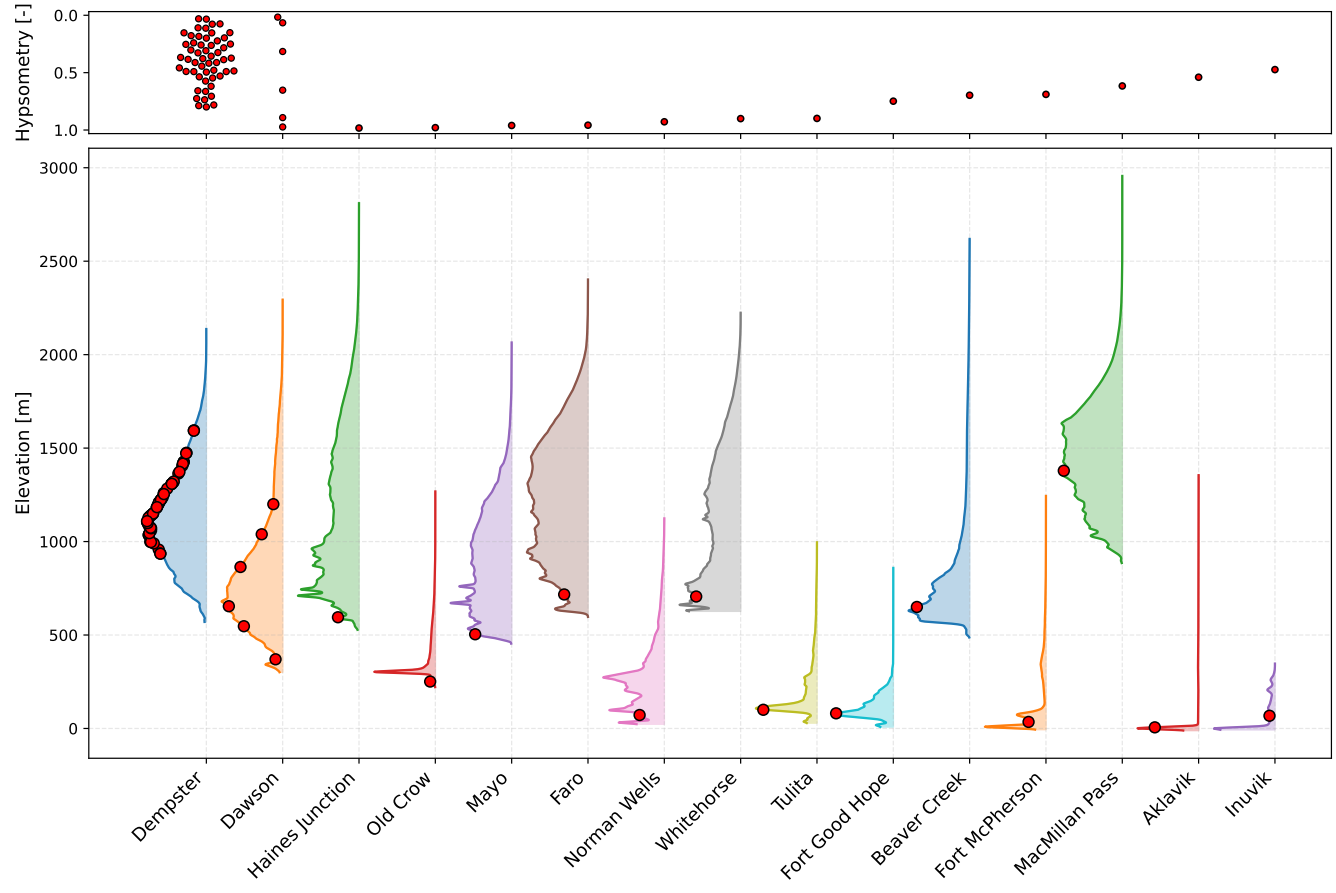

Figure 2. Local elevation distribution around each station from the study area (Dempster), the first testing area (Dawson), and the second testing area, made of 13 ECCC/NAVCAN weather stations (ranging from Haines Junction to Inuvik, sorted by decreasing hypsometry). The elevation and hypsometry of each station are indicated by a red dot.

Note that at the latitude of the study area, the reanalysis grid cell approximately corresponds to a $46\,\mathrm{km} \times 20\,\mathrm{km}$ cell for ERA5, and $59\,\mathrm{km} \times 30\,\mathrm{km}$ for JRA-3Q. We downscale all reanalysis products to the stations' locations and elevations while accounting for local topography using GlobSim. Furthermore, we acquire pressure-level air temperature T_{pl} for a full column above each valley from the highest station upwards, at each available pressure level. For both products, we also interpolate single-level $2\,\mathrm{m}$ surface temperature T_{sur}. This is now automated with the addition of the new DReaMIT module into GlobSim.

https://doi.org/10.5194/egusphere-2025-5512
Preprint. Discussion started: 6 February 2026

3.3 Temperature inversion model

3.3.1 Basic structure

Pozsgay and Gruber (2025) demonstrated that downscaled reanalysis data, both single-level surface temperature T_{sur} and pressure-level temperature T_{pl}, fail to capture the full vertical profile of surface-based inversions. T_{pl} generally performs better at approximating the observed temperature than T_{sur} at higher elevation, while the use of T_{sur} is preferable at lower elevation, in agreement with the previous comment about the lack of reliability of pressure level reanalysis data below grid level.

To bridge the gap between the two reanalysis variables and their non-intersecting domains of reliability, a dynamic model of temperature inversions was proposed in Pozsgay and Gruber (2025). This model was calibrated for sites in the vicinity of Dawson City, Yukon, Canada, an area subject to strong temperature inversions. The model was shown to predict air temperature better than either T_{pl} or T_{sur}, for virtually any combination of elevation, time, and reanalysis product.

Thanks to the full hourly-downscaled vertical profile of air temperatures above each valley, the upper-troposphere lapse rate is computed and updated hourly. The linear relation can be extrapolated to the grid level and the station's elevation, where we define $T_{\mathrm{lapse\ grid}}$ and $T_{\mathrm{lapse\ station}}$, respectively. The difference between the surface temperature given by reanalysis and the would-be temperature without any inversions at the grid level is given by $DT = T_{\mathrm{sur}} - T_{\mathrm{lapse\ grid}}$. The equivalent definition at the station's elevation reads $DT_{\mathrm{station}} = T_{\mathrm{obs}} - T_{\mathrm{lapse\ station}}$, which corresponds to the SBI_{mag} metric from Noad et al. (2023). The former model simply states that the inversion's strength α is a linear function of the elevation z,

$$DT_{\mathrm{station}} = \alpha(z) \cdot DT + \beta(t)\,, \tag{1}$$

where the function β is a pure temporal regional reanalysis bias, and only depends on the reanalysis product, the study area, and the seasonality, not on the elevation. Note that the temporality of the inversion strength is fully characterized by the temporality of DT, a derivative of reanalysis variables.

3.3.2 Hypsometry

This manuscript aims to find a parameterization for the inversion model that is more general than the one proposed in Pozsgay and Gruber (2025). There, temperature inversions are successfully modelled, but the number of weather stations are limited and local calibration cannot be spatialized. Indeed, the calibration used for Dawson City is not suitable for this study area (Noad et al., 2025). The main reason is that cold-air pooling is not driven by absolute elevation (even though highly correlated), but rather relative elevation compared to the surrounding topography.

A simple first step would be to explore the same model but to replace absolute with relative elevation. However, a number of questions remain. First, of all, the notion of lowest point itself is ambiguous, as it depends on the radius around the station. Then, both a valley bottom and a point in the middle of a flat tundra will receive the same null relative elevation, even though the temperature inversion dynamics differ vastly between these two cases. Furthermore, such a definition does not provide any information on higher elevations. Two points can share a similar relative elevation but be close to the bottom of a steep,

https://doi.org/10.5194/egusphere-2025-5512
Preprint. Discussion started: 6 February 2026

narrow, and deep valley on the one hand, or be on a gentle ridge on the other hand. Once again, one does not expect these two configurations to lead to similar inversion dynamics.

Thus, a suitable and generic model of temperature inversions should rely on a variable transformation of the elevation that accounts for neighbouring topographic conditions. For the rest of this paper, we will explore the use of the hypsometric position h of a point within a given surrounding area, in the same fashion as Cao et al. (2017). This new variable will be bounded between 0 and 1 for the highest and lowest points in the area, respectively.

The calculation of h requires a digital elevation model (DEM). We download the Arctic DEM data (mosaics) for a radius of at least $50\,\mathrm{km}$ around every point in the study area (Porter et al., 2023). This dataset is available at a $2\,\mathrm{m}$ resolution, but we choose to work with one of $10\,\mathrm{m}$ as we are not interested in microtopography but relative cell elevation compared to other cells in a large radius. We study the influence of selecting smaller areas in Appendix A, where we motivate the choice of an ideal radius based on empirical optimization. Next, for each point with coordinates $\boldsymbol{x}_0$, the hypsometry is computed by looking at all cells c (coordinates $\boldsymbol{c}$) within a radius d (we will take $d = 50\,\mathrm{km}$), and corresponds to the fraction of points with higher elevation within that area,

$$h(\boldsymbol{x}_0) = \frac{\sum_c \theta(d - |\boldsymbol{c} - \boldsymbol{x}_0|)\theta(z_c - z_0)}{\sum_c \theta(d - |\boldsymbol{c} - \boldsymbol{x}_0|)}\,, \tag{2}$$

where θ is the Heaviside step function. In particular, $\theta(d - |\boldsymbol{c} - \boldsymbol{x}_0|)$ selects DEM cells within the predefined area, and $\theta(z_c - z_0)$ further selects the ones with elevation z_c higher than the center point elevation z_0. We study the influence of applying a $2d$ Gaussian weight with varying standard deviation (between 1 and $30\,\mathrm{km}$) in Appendix A. With the definition of the hypsometric position given by Eq. (2), we have $h \in [0, 1]$, and

$$h = \begin{cases} 0 & \text{on top of the highest summit}\,, \\ 1 & \text{at the bottom of the lowest valley}\,. \end{cases} \tag{3}$$

The model proposed in this study substitutes the elevation z for the dimensionless and bounded hypsometric position h used in Cao et al. (2017). There, it was used in combination with the multiresolution valley bottom flatness (MRVBF) index v (Gallant and Dowling, 2003), but we discard it here as we will find it to be superfluous in our analysis. The hypsometric model then takes the form,

$$T_{\mathrm{hyps}}(h, t) = T_{\text{lapse station}} + \alpha_{\exp}(h) \cdot DT + \beta(t)\,. \tag{4}$$

with

$$\alpha_{\exp}(h) = \alpha_{\text{intercept}} + (\exp(\alpha_{\text{slope}} \cdot \mathrm{h}) - 1)\,, \tag{5}$$

$$\beta(t) = \beta_{\text{amplitude}} \cdot \cos(2\pi(t - t_*)) + \beta_{\text{bias}}\,, \tag{6}$$

where t stands for the yearly time fraction. The wide regional reanalysis air temperature bias is independent of topography and seasonally variable, hence it is described by the sinusoidal function $\beta(t)$. Note that we modify the linear α into an exponential

https://doi.org/10.5194/egusphere-2025-5512
Preprint. Discussion started: 6 February 2026

function (which remains bounded since h itself is bounded within $[0,1]$). For small values of hypsometric position ($h << 1$), we recover the same linear α as the one of Pozsgay and Gruber (2025) to first order, since $\alpha_{\exp}(h) = \alpha_{\text{slope}} \cdot h + \alpha_{\text{intercept}} + \mathcal{O}(h^2)$. The exponential correction only affects hypsometric values closer to 1, corresponding to points located in lower terrain, where inversions are likely stronger. The flowchart of the model is presented in Fig. 3. In practical application, DReaMIT requires only two inputs: (1) a digital elevation model to compute hypsometric position, and (2) reanalysis air temperatures for the neighbouring grid cells. Once calibrated, the model produces spatially-continuous hourly temperature fields across complex terrain, enabling inversion-driven corrections even at sites lacking station data, provided surrounding terrain shows meaningful valley–ridge relief.

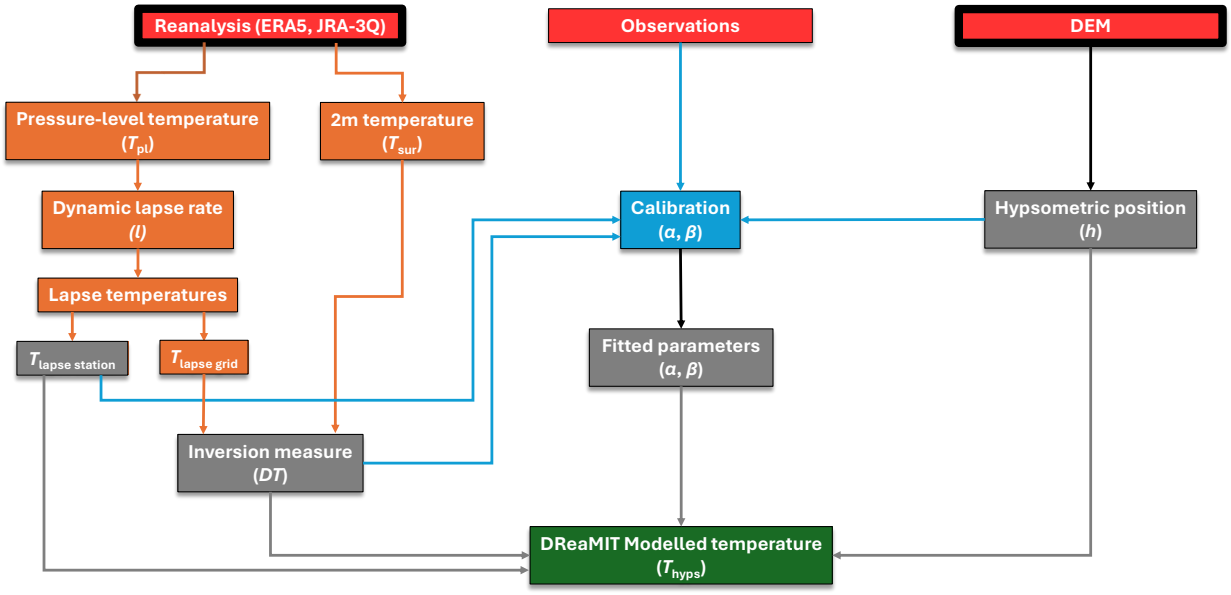

Figure 3. Flowchart of the DReaMIT hypsometric model. The input data for this study appear on the first row in red, the intermediate reanalysis steps in orange, the direct model input in grey, and the model output in green. The calibration performed in this study is shown in blue. For future cases when calibration is no longer needed, the user will only need to provide the data corresponding to cells with a thick black outline.

https://doi.org/10.5194/egusphere-2025-5512
Preprint. Discussion started: 6 February 2026

3.3.3 Calibration

The main advantage of a model based on hypsometric position, such as the one given in Eq. (4), is its range of applicability. Here, we no longer need to calibrate the model for each area, or even each valley; instead, we will calibrate it for both valleys of the study area at once (but independently for each reanalysis).

The data used to calibrate the model is selected to cover the widest temporal and elevational range. For each selected time, all stations with a valid record contribute to the calibration dataset. We select the maximum period for which all stations are operational, corresponding to a full year (minus 2 weeks in August, which does not bias the calibration since virtually no inversions are recorded then), and keep data at a 2 h frequency. Details can be found in Table 1. However, we will nevertheless assign a more important weight to the existing August datapoints so that each month is equally represented. Moreover, we also account for the non-uniform distribution of the hypsometric positions h in the interval $[0, 1]$ by assigning a weight to each station from Gaussian kernel density estimation (KDE). We will then perform a least-square optimization procedure to find the best model parameters for the calibration dataset. Finally, we will apply the model to the full dataset and evaluate its performance.

	WS01	WS02
Start (UTC)	2023-08-23 19:00	2023-08-24 19:00
End (UTC)	2024-08-09 15:00	2024-08-04 01:00
Frequency	2 h	2 h
Data used for calibration	36 %	37 %

Table 1. Subset of the observation dataset used for model calibration. The full dataset extends over multiple years for some stations, but we choose to keep a one-year window where all stations were recording for the calibration, roughly corresponding to a third of the dataset.

A least-square optimization is performed for all parameters of the model found in Eq. (4), on the calibration subset defined in Table 1. The calibration results can be found in Table 2.

3.3.4 Mean alpha

To demonstrate the advantage of using hypsometric position h over (relative) elevation, we will focus on the main quantity of the model, α, i.e. the factor quantifying the strength of inversion. This factor is purely time-independent, as opposed to all other quantities in the inversion model. In order to visualize the observed α as a function of (relative) elevation, and then of hypsometry, let us start by noting that Eq. (4) can be rewritten in the following form,

$$\alpha = \frac{DT_{\text{station}} - \beta}{DT}, \tag{7}$$

for every datapoint used for the model calibration. It is more meaningful to average this formula over time to get a mean observed factor. The calibration dataset is made of data that is uniformly distributed over a 1-year span (up to a small gap taken

https://doi.org/10.5194/egusphere-2025-5512
Preprint. Discussion started: 6 February 2026

into account in the calculations but omitted here for the sake of the argument), and hence the temporal average corresponds to a yearly mean. Let us denote the yearly mean of a quantity $\mathcal{Q}$ with $\overline{\mathcal{Q}}$,

$$\alpha_{\text{observed}} = \frac{\overline{DT}_{\text{station}} - \overline{\beta}}{\overline{DT}}, \tag{8}$$

and note that because of the oscillatory nature of the reanalysis bias $\beta(t)$, we have $\overline{\beta} = \beta_{\text{bias}}$, whose value is updated and fitted separately for each case.

4 Results

4.1 Fitted parameters

The relationship between hypsometric position and elevation depends on the area from which the hypsometric position is calculated, and the chosen weighting scheme. We find that the best fit is obtained when no weighting is performed (see Appendix A), which simplifies the approach.

We calibrate the model from Eq. (4) with a subset of the full dataset (see Table 1), where a least-squared fitting method is applied. The input data needed to calibrate the model are the hypsometric position on one side, which is calculated from a DEM, and reanalysis data on the other side (we use both ERA5 and JRA-3Q). The best fit parameters and their uncertainty are reported in Table 2. Note that we also fit the model in the absence of the reanalysis bias correction term $\beta(t)$. This reduces the model performances but increases its versatility and applicability in certain cases presented in the Discussion (Section 5).

		With $\beta(t)$				Without $\beta(t)$			
Parameter	Unit	ERA5		JRA-3Q		ERA5		JRA-3Q	
α_{slope}		0.732	(0.2 %)	0.753	(0.3 %)	0.728	(0.2 %)	0.752	(0.3 %)
$\alpha_{\text{intercept}}$		0.449	(0.4 %)	0.525	(0.4 %)	0.352	(0.3 %)	0.478	(0.3 %)
$\beta_{\text{amplitude}}$	°C	0.918	(1.7 %)	0.796	(2.1 %)	–		–	
t_*		0.958	(0.2 %)	0.945	(0.3 %)	–		–	
β_{bias}	°C	1.181	(1.0 %)	0.229	(4.9 %)	–		–	

Table 2. Best fit parameters (and their relative uncertainties in parentheses) for the calibration of the model given by Eq. (4). The model is also fitted in the absence of the reanalysis bias correction term $\beta(t)$.

The temperature inversion model REDCAPP (Cao et al., 2017) makes explicit use of both hypsometric position h and MRVBF index v. We find that the Akaike and Bayesian information criteria (AIC and BIC, respectively) do not improve when explicitly accounting for v in the model, which motivates the functional form adopted in Eq. (4), where the temperature inversions only depend on the hypsometric position h.

https://doi.org/10.5194/egusphere-2025-5512
Preprint. Discussion started: 6 February 2026

4.2 Comparing different models

We present a comparative analysis on the full northcentral Yukon valleys WS01 and WS02 dataset, which aims to put the performance of the new hypsometric model in context by comparing it to various other models in Fig. 4. The first model ('Dawson') is the inversion model proposed in Pozsgay and Gruber (2025), with their calibrated parameters. The second row, labelled 'Absolute elevation', uses the same model but with parameters specifically calibrated for the combined WS01 and WS02 valleys. The third row uses relative elevation with respect to valley bottom instead of absolute elevation, and the final row is the hypsometric model of this study. The 'Dawson' model and parameters perform very poorly in this study area with a coefficient of correlation of 0.17 for ERA5 but even as low as -0.60 for JRA-3Q, confirming what was already known, i.e., it is a model that needs to be calibrated locally, which is done in the second row with much better agreement ($R^2 = 0.76$ and 0.73 respectively). However, there is a clear distinction between the valleys, with values from WS01 above those of WS02. This is even more visible when looking at relative elevation, where the decoupling between the two valleys becomes so large that the model is clearly inappropriate. However, when turning to the more intricate variable transformation of elevation that hypsometry is (fourth column), we see that both valleys align, and a single model can now be applied confidently in different geographical locations. The correlation coefficient of the mean observed α over the full dataset with respect to the modelled α is equal to $R^2 = 0.93$ in the case of ERA5, and 0.87 for JRA-3Q.

Finally, we also perform single-valley calibration, and demonstrate the stability of the results when applied to the other valley in Appendix B. This constitutes a first step towards demonstrating the spatialization power of the model.

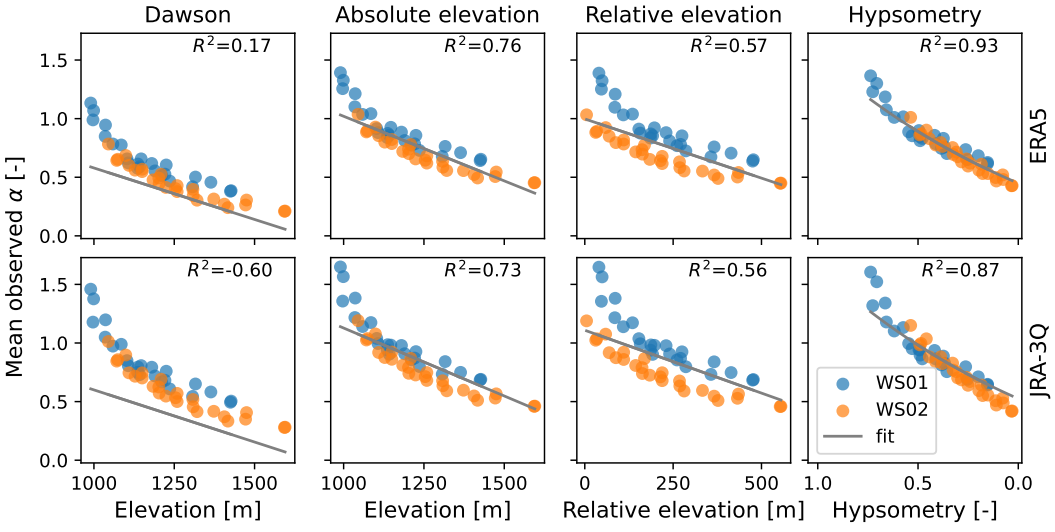

Figure 4. Mean observed and modelled values of the factor $\alpha(h)$ for various temperature inversion models and reanalyses.

https://doi.org/10.5194/egusphere-2025-5512
Preprint. Discussion started: 6 February 2026

4.3 Application to other sites

4.3.1 Dawson area

To evaluate the performance of the hypsometric model Eq. (4) outside the study area we make use of the weather data from the stations around Dawson City, Yukon, located more than $100\,\mathrm{km}$ away from the two Dempster Highway valleys where the hypsometric model is calibrated. For each of the five stations, we download reanalysis data, scale it to the point locations, compute the lapse rate of their respective air columns, and download the ArcticDEM locally to transform elevation information into hypsometric position h.

The results are shown in Fig. 5 below (left panel), and in Appendix C. For each station, we present the statistical metrics MAE and R^2 as a function of hypsometry, for the new hypsometric model, compared to the worst of the surface and pressure-level temperatures given from reanalysis data (downscaled using GlobSim (Cao et al., 2019)). We compare to the worst of T_{pl} and T_{sur} since we cannot know a priori which will be best (Pozsgay and Gruber, 2025). A more complete comparison is presented in Appendix C. Note that we average results for ERA5 and JRA-3Q and present a relative change rather than absolute metrics. Positive values indicate better predictions from the model compared to reanalysis. However, it is interesting to note that the hypsometric model (whose parameters are given in Table 2 and set once and for all) predicts air temperature more consistently than either surface or pressure-level reanalysis data. We recall the fact that the pressure-level reanalysis data performs best at higher elevation (low h, milder inversions) while the strong inversions at the valley bottom (low elevation, high h) are better represented by the surface temperature of the reanalysis data.

In the situation where the user wishes to apply the model to an area where the reanalysis bias could be different than the one from Table 2 (column with β) and where no weather stations are available to calibrate β, a good alternative is to use the model calibrated without the β term (column without β of Table 2). In this case, the results are slightly worse than with the β term (except for the low h stations), but continue to outperform the reanalysis products. Once again, when no reanalysis correction is applied for the model and T_{pl} and T_{sur}, results are negatively affected but maintain the same order of magnitude. The same conclusions apply.

4.3.2 Network of northern ECCC stations

In this Section, we perform a similar analysis, but extend the testing further away, comparing the model results to the observations at 13 ECCC/NAVCAN weather stations across the Yukon and the Northwest Territories (NWT). Results are reported on the right panel of Fig. 5. The horizontal axis represents the hypsometry, modulated by the potential to drive temperature inversions. If we write dz the difference in elevation between the 90^{th} and 10^{th} percentiles in the area around each point location, then the hypsometric range is given by the product $h \cdot dz$.

For stations with lower hypsometric range, i.e., milder topography, the hypsometric model (with and without reanalysis bias correction) offers better predictions than reanalsysis data. However, it has poorer performances for intermediate values of the hypsometric range, especially for Tulita, Old Crow, and Norman Wells. When the hypsometric range increases further, the

https://doi.org/10.5194/egusphere-2025-5512
Preprint. Discussion started: 6 February 2026

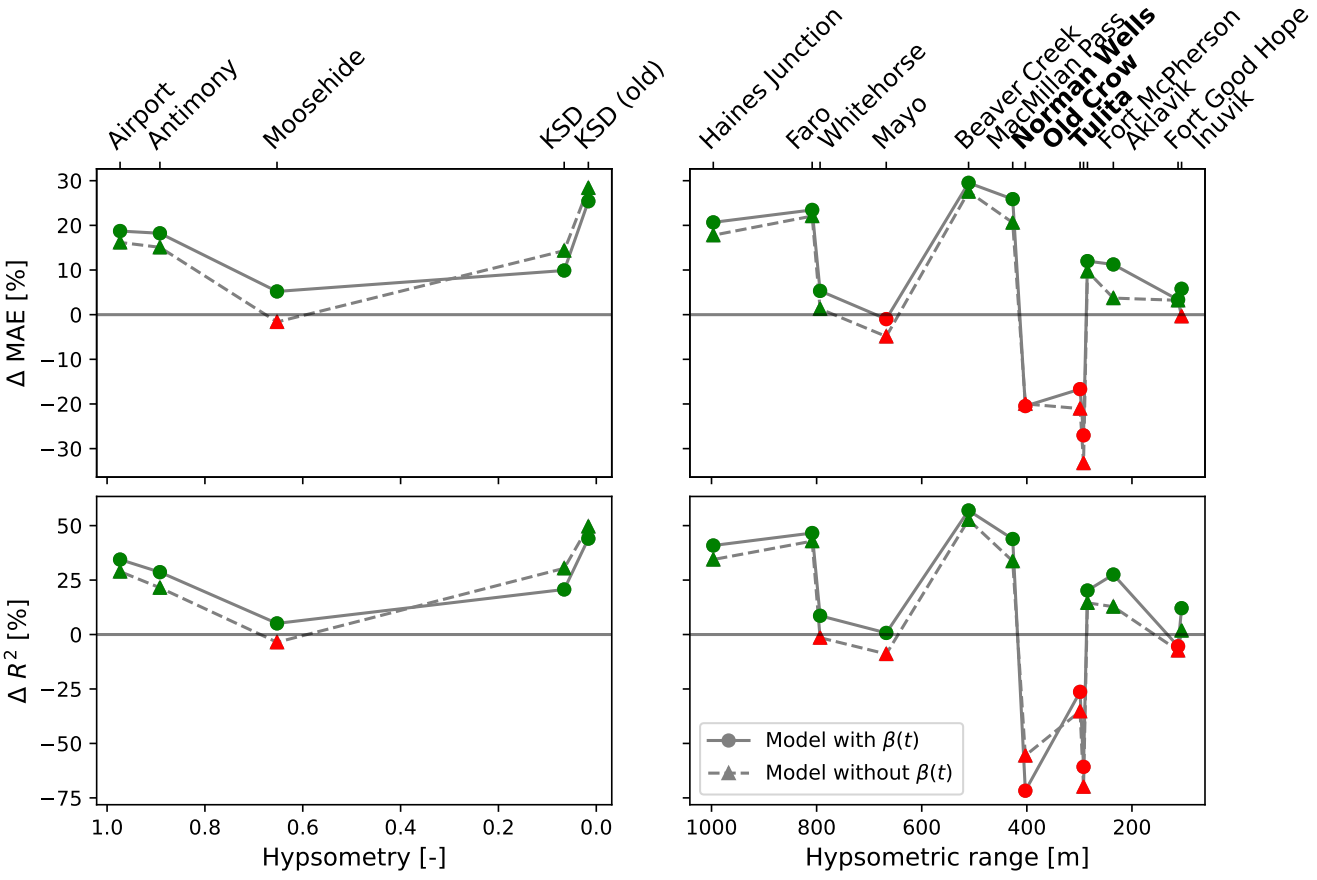

Figure 5. Statistical metrics for model versus observations. The hypsometric model calibrated with and without the reanalysis bias term $\beta(t)$ is compared to the worst of T_{pl} and T_{sur} (respectively corrected or not with $\beta(t)$) for MAE and R^2. Green markers indicate better predictions from the model than reanalysis, while red is worse. Stations where the hypsometric model performs worst overall appear in bold. (left) The 5 locations around Dawson City. (right) Same metrics for the 13 ECCC/NAVCAN weather stations in the Yukon and Northwest Territories. The hypsometric range is the product of (a) the hypsometric position and (b) the elevation range excluding outliers (the elevation difference between the 90^{th} and 10^{th} percentiles in the area around the point location).

best increase in reliability is observed, reaching a maximum at Beaver Creek with a 30 % and 57 % lowering of the MAE and $(1 - R^2)$, respectively. Particularly good performances are also observed at MacMillan Pass, Faro, and Haines Junction.

https://doi.org/10.5194/egusphere-2025-5512
Preprint. Discussion started: 6 February 2026

5 Discussion

5.1 Use of hypsometry instead of (absolute) elevation

The new surface-based inversion model proposed in this study spatializes the model of Pozsgay and Gruber (2025) while making the calculation of the REDCAPP laspe rate (Cao et al., 2017) dynamic. The factor that controls the strength of the temperature inversion events, α, is modified by considering hypsometric position instead of elevation. With this choice, we successfully unify the functional form of α as a function of a variable transformation of elevation for dissimilar valleys (Fig. 4). A single calibration can now be performed simultaneously for the two valleys (WS01 and WS02) of the study area, and the resulting model is reliable in both valleys. To show that the model is indeed robust against spatialization, we perform cross-valley calibrations and find it to be reliable there too (Fig. B1).

5.2 Physical interpretation of nonlinearity

Another improvement compared to the 'Dawson' model is the exponentiation of the elevation variable, instead of the linear form of α. The functional form of the proposed α_{exp} in Eq. (5) reduces to the linear form of Pozsgay and Gruber (2025) for locations with $h << 1$, while allowing for the representation of stronger inversions when $h \lesssim 1$, a frequently observed phenomenon.

SBIs in high-latitude valleys often exhibit non-linear lapse-rate profiles (Tikhomirov et al., 2021), where strong temperature stratification near the surface transitions to weakly stratified or isothermal layers above (Mayfield and Fochesatto, 2013). This pattern was observed in the subarctic valleys used to calibrate this model (Noad and Bonnaventure, 2025). During an SBI, lapse rates typically decayed exponentially within the first roughly $150\,\mathrm{m}$ where they often exceeded $25\,^{\circ}\mathrm{C\,km^{-1}}$ within the lowest $60\,\mathrm{m}$ and then approached isothermal above $150\,\mathrm{m}$. In extreme cases, there was as much as $8\,^{\circ}\mathrm{C}$ temperature increase over $19\,\mathrm{m}$ between the valley bottom and adjacent slope site (Noad and Bonnaventure, 2025).

The exponential function therefore better captures the observed behaviour of mean inversion strength (last column of Fig. 4), while being safe from unwanted divergence given the boundedness of the hypsometric position ($h \in [0, 1]$). Nonetheless, the correction is still slightly underestimating the inversion strength for the points with higher hypsometry (last column of Fig. 4). For the readers who might be surprised not to find a better fit of the mean observed α, we would like to reiterate that the fit presented there is the full model calibrated with hourly data in both valleys, and not a direct fit of mean yearly observed α.

5.3 Spatial transferability and scope of applicability

The model described by Eq. (4) was tested across a wide geographical range in Yukon and Northwest Territories, encompassing topographic diversity (Fig. 2). The hypsometric model is more versatile than any of the reanalysis temperatures, even far from the calibration study area, which proves the success of this new formulation. Model performance in Whitehorse, Haines Junction, and MacMillan Pass, which are locations that experience weaker and more transient inversions than the subarctic valleys along the Dempster Highway (Lewkowicz and Bonnaventure, 2011; Noad et al., 2023; Garibaldi et al., 2024), remained

https://doi.org/10.5194/egusphere-2025-5512
Preprint. Discussion started: 6 February 2026

surprisingly strong. This suggests that while the model was calibrated for more continental Dempster valleys, it captures the underlying structure of SBIs well, and that its transferability extends to regions with comparable hypsometric ranges. In these settings, the model appears to represent topographic constraints on cold-air pooling processes that develop within landscapes characterized by large hypsometric range. Although the frequency and intensity of SBIs are less at Whitehorse, MacMillan Pass, and Haines Junction, their structure likely resembles those of the Dempster sites.

However, the model's transferability has limits. First of all, the inclusion of a reanalysis bias correction term β creates issues. Indeed, reanalysis bias is not uniform in time (see Fig. 7 of Fiddes and Gruber (2014)), but more importantly, it varies in space while the model explicitly assumes a spatially-independent $\beta(t)$. Such a term increases model performances in a region of applicability, but is not appropriate for applications elsewhere. Instead, for such locations, we recommend either recalibrating β locally if nearby weather stations exist, or using the model calibrated without the β term (right column of Table 2), which increases the model's versatility. We showed that model performances are only minimally affected in the absence of reanalysis bias correction, demonstrating that the spatial scale at which the model can be applied is not limited by the scale over which the reanalysis bias varies. Second, the model performed poorly for certain ECCC stations, including Tulita, Old Crow, and Norman Wells. As shown in Fig. 2, these locations correspond to those with higher hypsometry, while not in a mountain area. The topography for these areas is mainly flat (the elevation distribution peaks around the elevation of the lowland), and hence, any slight elevation variation has a disproportionate effect on the hypsometry. This is a limiting case of the model. Note that for Old Crow and Tulita, the calculated value of h is close to 1, but the stations are nowhere close to being at the bottom of a deep valley. This constitutes an extreme topographic situation where the model might not be suitable. These exceptions highlight the limits of the domain: in extremely flat, river-dominated terrain, hypsometry becomes unstable and river-generated warm anomalies overwhelm the topographic signal the model relies on. In this context, the inclusion of the MRVBF in a more intricate model might mitigate this undesirable effect by better distinguishing flat from incised terrain.

A related limitation arises in generally flat areas with a low range in hypsometry. Attempts to incorporate a modified variable, a bounded version of the hypsometric range $h \cdot dz$, which accounts for the topographic potential to sustain inversions did not substantially improve performance. Similar challenges have been reported in other lapse rate-based downscaling studies, where the absence of pronounced topographic relief often reduces the prediction of elevation-derived parameters (Fiddes et al., 2022). In such environments, microtopographic indices such as MRVBF used in REDCAPP (Cao et al., 2017) may provide complementary information on the structure of SBIs and resulting elevational patterns of air temperature. This metric, or something similar, could be used as a mechanism, to limit hypsometry closer to 0 in these flat areas.

Our results indicate a clear domain limit: stations situated on low-relief floodplains on the leeward side of mountain ranges (e.g., Norman Wells, Tulita, Old Crow) exhibit degraded performance relative to incised valleys. In such settings, the gravitational pooling that sustains surface-based inversions (SBIs) is weak because slopes and basin geometry are minimal; small uncertainties in hypsometry are therefore amplified, especially when the seasonal temperature contrast DT is large. Leeward positioning further reduces inversion persistence via mechanically-driven mixing and episodic flushing (Hrebtov and Hanjalić, 2017; Dice et al., 2024), while riverine processes (late freeze-up, open water, advective heat) can imprint non-orographic thermal anomalies during transition seasons (Park et al., 2020; Prowse et al., 2007). Together, these factors yield a near-surface

https://doi.org/10.5194/egusphere-2025-5512
Preprint. Discussion started: 6 February 2026

temperature structure that is not primarily topography-controlled, and our hypsometry-based correction can over-adjust. We therefore recommend caution for leeward floodplain sites, particularly those proximal to major rivers. In this configuration, the better-performing air temperature is T_{sur}. This framing clarifies that the model performs as intended in incised, terrain-controlled valleys, while transferability is limited where floodplain and river energy budgets dominate boundary-layer thermodynamics.

5.4 Scale effects on hypsometry

We focused some effort into determining the best radius around each point location to compute the hypsometric position, and concluded that even though there might exist intermediate radii for specific configurations, the most robust option was to consider a radius of $50\,\mathrm{km}$, with no weighting. Recent studies have shown that the interplay between large-scale synoptic conditions and local radiative and cold-air drainage processes is scale-dependent, with larger valley systems having a more complex interaction between the two mechanisms (Crosman and Horel, 2017; Hughes et al., 2015; Sheridan, 2019). This suggests that the radius that performs best empirically ($50\,\mathrm{km}$) is of the order of the physical scale at which local drainage and synoptic influences control SBI strength, providing a physical rationale for the effective use scale for hypsometeric position used in our model.

We showed the existence of a hierarchy of scales, with a local minimum in model performance reached for local valley scales (roughly $5\,\mathrm{km}$ radius for the study area), but a global and potentially location-independent best fit at larger scales (Appendix A). However, the physical scales controlling cold-air pooling and inversion persistence in the western Canadian Arctic may differ from those in other regions, and thus the relationships should be interpreted cautiously. Moreover, considering larger areas in the hypsometry calculation is yet to be tested for various topographic conditions across the western Canadian Arctic.

6 Conclusion

The hypsometric temperature inversion model proposed in this study is a spatialized and dynamic surface-based inversion model. Previously, it was shown that there exists a simple relationship between inversion strength and elevation for a specific area. However, this relationship varies spatially, meaning it would need recalibration for every new location. Here, we find a variable transformation of elevation (hypsometry) that preserves the shape of the inversion strength (function α) across dissimilar valleys. This new approach reuses one of the REDCAPP (Cao et al., 2017) parameters while disregarding the valleyness index (MRVBF), which was shown not to decrease the amount of information lost by the model. The DReaMIT hypsometric model combines the spatialization of REDCAPP and the dynamic lapse rate calculations of Pozsgay and Gruber (2025), while retaining a simple expression and a minimal number of dependent variables.

We then started to test the model transferability by showing the high performance of cross-valley calibration, i.e., calibrating the model in a valley and testing it in another. This first step towards a proof of the spatialization power of the model was then followed by a larger test in the Dawson City area, and across numerous ECCC stations in the Yukon and Northwest Territories. It was found to be the most robust and reliable model of air temperature when compared to raw reanalysis data and the ‘Dawson’

https://doi.org/10.5194/egusphere-2025-5512
Preprint. Discussion started: 6 February 2026

model. This does not mean that the hypsometric model always performs best, but rather that it is, on average, the preferred option. However, we issue recommendations for the best use of this model: (a) use when the hypsometry is well-defined, i.e., when small variations in elevation do not lead to dramatic variations in h, (b) for applications outside of the western Canadian Arctic, recalibrate the reanalysis bias β locally with weather station data when available, or use the 'no-β' version of the model otherwise. With this caveat in mind, we thus present a reliable, spatialized, and dynamic model of temperature inversions for the mountainous western Canadian Arctic.

Code and data availability. The current version of DReaMIT is available as an integrated GlobSim module from the 'DReaMIT_demo' branch of the project https://github.com/geocryology/globsim under the license GNU General Public License v3.0. The exact version of the model used to produce the results used in this paper is archived on Zenodo under DOI: 10.5281/zenodo.17545268 (Pozsgay et al., 2025), as are input data and scripts to run the model and produce the plots for all the simulations presented in this paper. The observational data from the WS01 and WS02 valleys, and from the Dawson study area are also accessible there. The remaining observational data is from ECCC/NAVCAN. The reanalysis data is available from ECMWF and JMA for the ERA5 and JRA-3Q datasets.

Author contributions. Conceptualization: SG, VP, PB, NN. Data curation: VP, NN. Formal analysis: VP. Funding acquisition: PB, SG. Software: VP. Supervision: PB, SG. Visualization: VP, NN. Writing (original draft preparation): VP, NN. Writing (review and editing): PB, SG.

Acknowledgements. We would like to thank D. Cronmiller, P. Lipovsky, the Yukon Geological Survey (YGS), and Environment and Climate Change Canada (ECCC) for sharing their weather station data. We acknowledge the Northern Scientific Training Program by Polar Knowledge Canada, as well as field support from M. Garibaldi, S. Lamoureux, M. Codd, S. MacLean, R. Thiessen, and R. Nicholson. We would like to thank Nick Brown for his technical support with GlobSim. We would also like to acknowledge ECMWF and JMA for the ERA5 and JRA-3Q reanalysis data. This study was supported by the governments of Yukon (T00026926) and British Columbia (TP23PGE222), the Digital Research Alliance of Canada (772), as well as NSERC via PermafrostNet (NETGP 523228-18), CREATE LEAP (575207), Discovery Grant RGPIN-2020-04783, and Discovery Development Grant 110_2024_2025_Q1_4012.

Appendix A: Relative importance of the radius of the hypsometric position

The hypsometric position was defined in Eq. (2). We here study the influence of adding a $2d$ Gaussian weight modulating the typical spatial scale of the inversions. Here, we weigh each cell c with a Gaussian weight with standard deviation r,

$$h_r(\boldsymbol{x}_0) = \frac{\sum_c \omega(r, |\boldsymbol{c}-\boldsymbol{x}_0|)\theta(d-|\boldsymbol{c}-\boldsymbol{x}_0|)\theta(z_c-z_0)}{\sum_c \theta(d-|\boldsymbol{c}-\boldsymbol{x}_0|)\omega(r,|\boldsymbol{c}-\boldsymbol{x}_0|)}, \tag{A1}$$

https://doi.org/10.5194/egusphere-2025-5512
Preprint. Discussion started: 6 February 2026

where the weights are defined by

$$\omega(r, |\boldsymbol{c} - \boldsymbol{x}_0|) = \exp\left\{-\frac{|\boldsymbol{c} - \boldsymbol{x}_0|^2}{2r^2}\right\}. \tag{A2}$$

We can also compute the multiresolution valley bottom flatness (MRVBF) index (Gallant and Dowling, 2003), which is an index that parameterizes the valleyness of a given point.

The hypsometric position, as defined by Eq. (2) (or in Eq. (A1) for its weighed version), is a variable transformation of the absolute elevation. It carries information not only on the elevation of the point of interest, but also on the neighbouring terrain, or neighbouring cells if the terrain is discretized, such as in a DEM. The choice of the radius within which elevation information is retained reflects the scale at which the processes happen. For small radii, the local topography bears more importance, whereas it is increasingly smoothed with increasing exponential weight radius.

For each Gaussian weight radius r, we perform the calibration and evaluate the goodness of fit by computing different statistical metrics: root mean square error (RMSE), mean absolute error (MAE), reduced chi-square (χ^2_{red}), coefficient of correlation R^2, and both Akaike and Bayesian information criteria (AIC and BIC respectively). They are compared to equivalent results for the case where no weight is applied, which is the optimal case (see Fig. A1). The results improve quickly with increasing radius r, up to $r \sim 5\,\mathrm{km}$, where the goodness of fit finds a local minimum. Further increasing the Gaussian weight radius leads to worse agreements with observations for the model calibration, until $r \sim 10\,\mathrm{km}$. After this maximum, all metrics improve again, and the limiting case where no weight is applied is found to lead to the best agreement between model and observations for the calibration dataset.

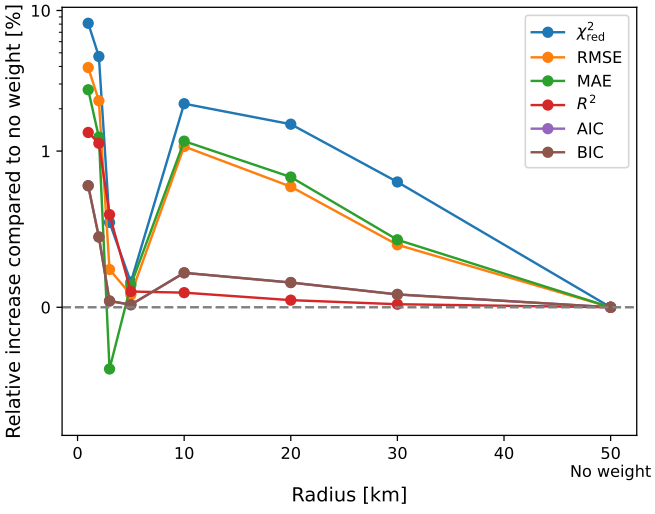

Figure A1. Comparison of the goodness of fit for the model calibration at different radii r, with respect to the limiting case without Gaussian weight.

https://doi.org/10.5194/egusphere-2025-5512
Preprint. Discussion started: 6 February 2026

We established the influence of the standard deviation of the $2d$ Gaussian weight r, not only in the value of h itself, but also in the performance of the inversion model. For each radius, reanalysis, and stations, the mean observed α_{exp} is computed and plotted in Fig. A2. The exponential line of best fit is obtained from the calibrated parameters of the model (see Table 2 for the parameters used in the last column labelled 'No weight'). The line of best fit is thus not obtained directly at the level of the mean α_{exp}. However, the values of the correlation coefficient R^2 in Fig. A2 correspond to the correlation between mean observed α_{exp} and modelled α_{exp}, i.e. for a dataset consisting of a single point per station. The value of R^2 starts as low as 0.30 and 0.29 for a radius of $1\,\text{km}$ for ERA5 and JRA-3Q, respectively, and steadily increase until $r = 10\,\text{km}$ where they reach $R^2 = 0.91$ and 0.84, respectively. Further increasing the radius, or even dropping the $2d$ Gaussian weights altogether, has little to no impact on the correlation coefficient. However, the best agreement here too is found when no weighting scheme is applied (where $92\,\%$ of the variability in the mean observed α_{exp} is explained by the model for ERA5, and $86\,\%$ for JRA-3Q). This further motivates our choice to focus our analysis on this case.

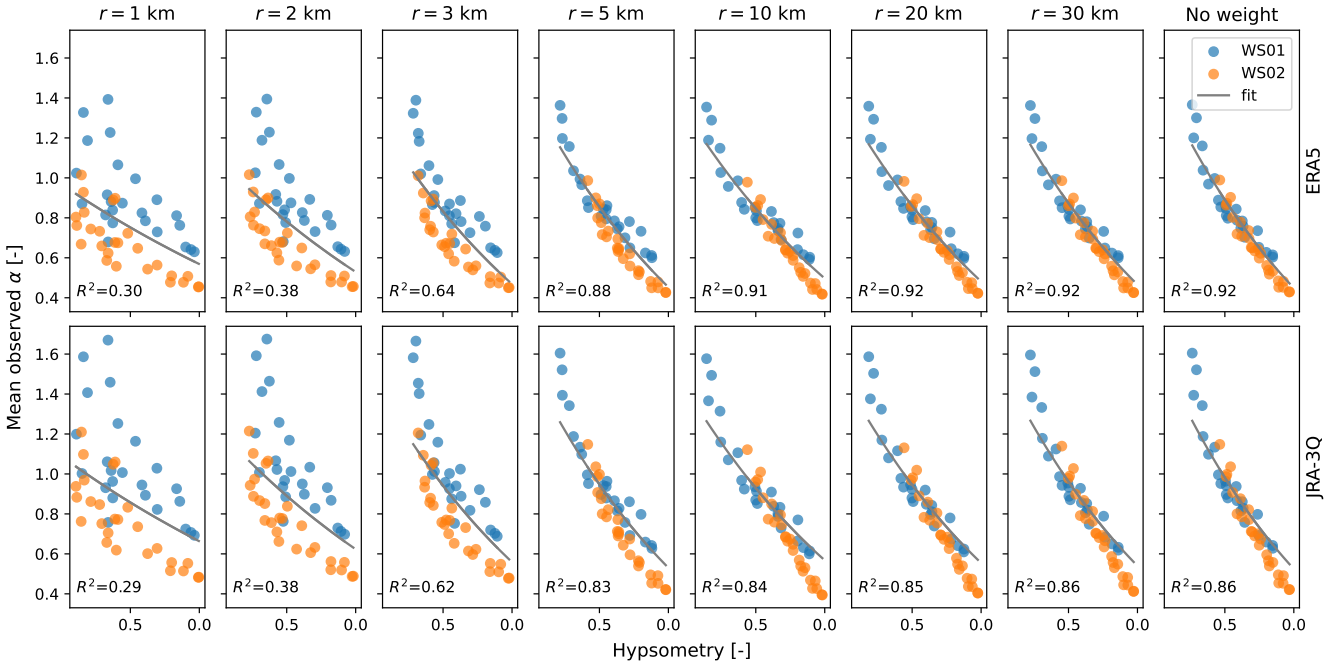

Figure A2. Mean observed values and calibration fit of the factor $\alpha_{\text{exp}}(h)$ for different radii and both reanalysis products.

Appendix B: Swapping valleys

We perform single-valley calibrations, and apply the resulting fitted parameters to the other valley for all data points and not just the calibration dataset. This allows us to show the applicability of the model outside of its calibration area. In Fig. B1, we

https://doi.org/10.5194/egusphere-2025-5512
Preprint. Discussion started: 6 February 2026

plot the same quantities as in the Section 4.2, i.e., mean observed α against hypsometry, overlaid by a line representing the modelled α, whose parameters are either calibrated for both valleys at once (first column), or for each valley independently (next two columns). The values of the coefficient of correlation are given for all stations in black, and for stations of individual valleys WS01 and WS02 in blue and orange, respectively.

When the model is only calibrated using a year of data from WS01 (second column), the calculated values of α (for all data points and not solely the calibration set) explain $85\,\%$ and $78\,\%$ (for ERA5 and JRA-3Q) of the variation of the mean observed α in the valley WS01, however this drops to respectively $79\,\%$ and $60\,\%$ when applying it to WS02. Now, the calibration of WS02 for WS01 performs much better, with correlation coefficients as high as 0.84 for ERA5 and 0.80 for JRA-3Q. Note that the cross-valley modelling is better when calibrating on WS02 because its own calibration results are better than WS01. Indeed, the shape of the mean observed α as a function of the hypsometric position h is more closely aligned with the exponential choice of fitting function for WS02 than WS01, and hence the poorer performance of the WS01-calibrated WS02 model is directly inherited from the relatively poorer performance of the WS01-calibrated WS01 model. The WS02-calibrated WS01 model (third column) is largely successful, which demonstrates the wider scope of this model, beyond its own calibration area.

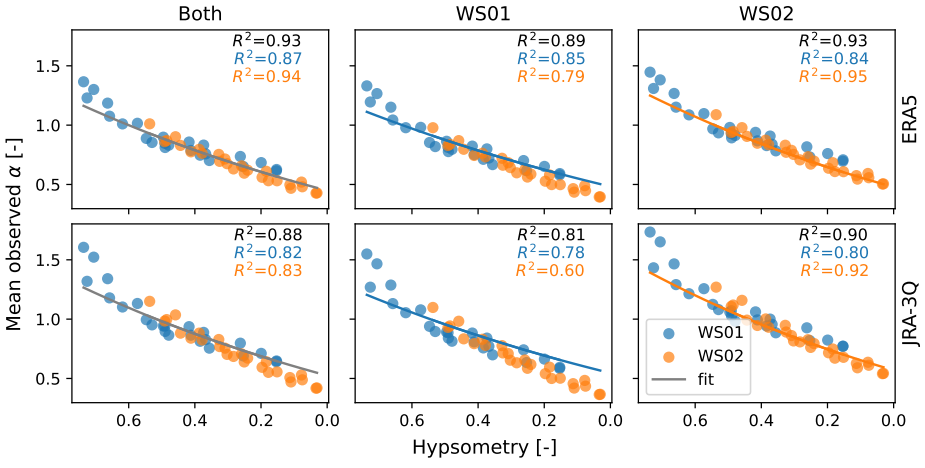

Figure B1. Mean observed and modelled values of the factor $\alpha(h)$ for a calibration over both valleys, or each valley individually, and for both reanalysis products.

Appendix C: Testing model performance relative to reanalysis products

We demonstrated that the model from Eq. (4), with and without the β term, globally outperformed the worst of the reanalyis products (corrected or not for the reanalysis bias) for the Dawson sites, and for most ECCC sites, except at intermediate to low hypsometric range. Here, we present the full picture and plot the values of MAE and R^2 with and without reanalysis

https://doi.org/10.5194/egusphere-2025-5512
Preprint. Discussion started: 6 February 2026

bias correction in Fig. C1, for the hypsometric model of Eq. (4), the reanalysis products (both T_{pl} and T_{sur}), and the Dawson model of Pozsgay and Gruber (2025). For the Dawson area (left), the 'Dawson' model performs the best, but this comes as no surprise, as it was specifically calibrated for the area, but was not designed to include any spatial generalizability. Whether reanalysis bias is corrected or not, the hypsometric model performs better than pressure-level temperature and worse than surface temperature for high h, while the opposite is true for low h.

For the ECCC stations (right panel of Fig. C1), stations with lower hypsometric range, i.e., milder topography, the temperature inversions are not as strong and the surface level reanalysis data is the one that performs the best, as expected. There, the hypsometric model exhibits similar values, and not worse than the pressure-level reanalysis data. For intermediate values of the hypsometric range, especially for Tulita, Old Crow, and Norman Wells, the hypsometric model seems to have poorer performance. However, it is then outperforming any raw reanalysis data at even higher values, especially for Beaver Creek.

We note that general conclusions are valid whether we look at the full hypsometric model, or the simplified one calibrated without the β term.

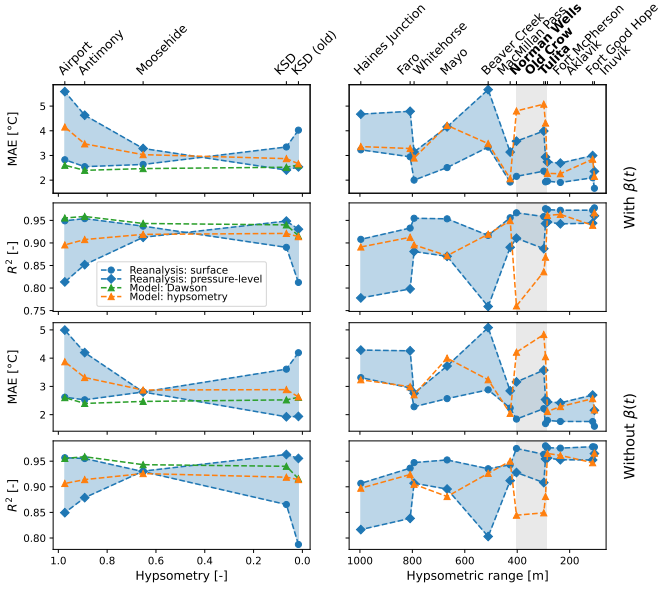

Figure C1. Statistical metrics for model versus observations. The hypsometric model calibrated with and without the reanalysis bias term $\beta(t)$ is compared to both T_{pl} and T_{sur} (respectively corrected or not with $\beta(t)$) for MAE and R^2. Stations where the hypsometric model performs worst overall appear in bold. (left) Comparison for the 5 locations around Dawson City, together with the model of Pozsgay and Gruber (2025) in orange. (right) Same metrics for the 13 ECCC/NAVCAN weather stations in the Yukon and Northwest Territories.

https://doi.org/10.5194/egusphere-2025-5512
Preprint. Discussion started: 6 February 2026

Appendix D: Study area temperature inversions

We compare the modelled air temperature given by Eq. (4) to the bias-corrected T_{sur} and T_{pl} (i.e., to which we subtracted β), for two stations from the WS01 valley. Those were chosen to represent low and high hypsometric positions. For the top row of Fig. D1, corresponding to high h, the best performing time series is the hypsometric model. The surface temperature is too low (MBE$=-1.60\,^{\circ}\mathrm{C}$), while the pressure-level temperature is too high, especially towards the lowest temperatures, resulting in poor MAE and R^2. Next, when turning to low h (bottom row), the hypsometric model is still the preferred option, but the pressure-level temperature has similar performances, except for a cold bias (MBE$=-0.95\,^{\circ}\mathrm{C}$). In this case, it is now the surface temperature that deviates at low temperatures, but presents a significant cold bias there. This comparison confirms the non-intersecting domains of applicability of T_{sur} and T_{pl} found in Pozsgay and Gruber (2025), while demonstrating the advantage of the hypsometric model.

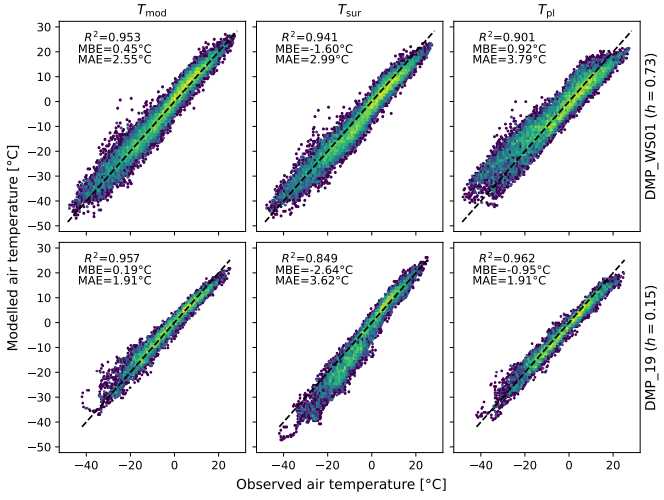

Figure D1. Parity plot of modelled versus observed temperatures for the two stations of diverse hypsometry from WS01 valley ($h = 0.73$ for the top row, and $h = 0.15$ for the bottom). We compare the results of the model to the bias-corrected T_{sur} and T_{pl}.

Appendix E: ECCC stations

https://doi.org/10.5194/egusphere-2025-5512
Preprint. Discussion started: 6 February 2026

Site	Station ID	Latitude [°]	Longitude [°]	Elevation [m]
Aklavik	52962	68.2233	−135.0056	6
Inuvik	51477	68.3039	−133.4831	68
Fort McPherson	52963	67.4069	−134.8597	35
Fort Good Hope	53580	66.2406	−128.6475	81
	27549	66.2422	−128.6442	82
Beaver Creek	53179	62.4103	−140.8689	650
Tulita	52967	64.9097	−125.5694	100
Norman Wells	50717	65.2814	−126.7986	72
	43004	65.2875	−126.7534	94
Whitehorse	50842	60.7094	−135.0672	706
	48168	60.7331	−135.0978	707
Old Crow	53023	67.5700	−139.8400	250
	26894	67.5706	−139.8392	251
Haines Junction	1556	60.7725	−137.5803	595
Mayo	51426	63.6164	−135.8683	504
Faro	8964	62.2075	−133.3758	717
MacMillan Pass	27339	63.2436	−130.0372	1379

Table E1. Network of ECCC/NAVCAN weather stations used for air temperature data over 10 years, between 2015-08-01 and 2025-07-31.

References

Cao, B., Gruber, S., and Zhang, T.: REDCAPP (v1.0): parameterizing valley inversions in air temperature data downscaled from reanalyses, Geoscientific Model Development, 10, 2905–2923, https://doi.org/10.5194/gmd-10-2905-2017, 2017.

Cao, B., Quan, X., Brown, N., Stewart-Jones, E., and Gruber, S.: GlobSim (v1.0): deriving meteorological time series for point locations from multiple global reanalyses, Geoscientific Model Development, 12, 4661–4679, https://doi.org/10.5194/gmd-12-4661-2019, 2019.

Crosman, E. T. and Horel, J. D.: Large-eddy simulations of a Salt Lake Valley cold-air pool, Atmospheric Research, 193, 10–25, https://doi.org/10.1016/j.atmosres.2017.04.010, 2017.

Daly, C., Halbleib, M., Smith, J. I., Gibson, W. P., Doggett, M. K., Taylor, G. H., Curtis, J., and Pasteris, P. P.: Physiographically sensitive mapping of climatological temperature and precipitation across the conterminous United States, International Journal of Climatology, 28, 2031–2064, https://doi.org/10.1002/joc.1688, 2008.

https://doi.org/10.5194/egusphere-2025-5512
Preprint. Discussion started: 6 February 2026

Dice, M. J., Cassano, J. J., and Jozef, G. C.: Forcing for varying boundary layer stability across Antarctica, Weather and Climate Dynamics, 5, 369–394, https://doi.org/10.5194/wcd-5-369-2024, 2024.

Draeger, C., Radić, V., White, R. H., and Tessema, M. A.: Evaluation of reanalysis data and dynamical downscaling for surface energy balance modeling at mountain glaciers in western Canada, The Cryosphere, 18, 17–42, https://doi.org/10.5194/tc-18-17-2024, 2024.

Etzelmüller, B.: Recent Advances in Mountain Permafrost Research, Permafrost and Periglacial Processes, 24, 99–107, https://doi.org/10.1002/ppp.1772, 2013.

Fiddes, J. and Gruber, S.: TopoSCALE v.1.0: downscaling gridded climate data in complex terrain, Geoscientific Model Development, 7, 387–405, https://doi.org/10.5194/gmd-7-387-2014, 2014.

Fiddes, J., Endrizzi, S., and Gruber, S.: Large-area land surface simulations in heterogeneous terrain driven by global data sets: application to mountain permafrost, The Cryosphere, 9, 411–426, https://doi.org/10.5194/tc-9-411-2015, 2015.

Fiddes, J., Aalstad, K., and Lehning, M.: TopoCLIM: rapid topography-based downscaling of regional climate model output in complex terrain v1.1, Geoscientific Model Development, 15, 1753–1768, https://doi.org/10.5194/gmd-15-1753-2022, 2022.

Fochesatto, G. J., Mayfield, J. A., Starkenburg, D. P., Gruber, M. A., and Conner, J.: Occurrence of shallow cold flows in the winter atmospheric boundary layer of interior of Alaska, Meteorology and Atmospheric Physics, 127, 369–382, https://doi.org/10.1007/s00703-013-0274-4, 2015.

Gallant, J. C. and Dowling, T. I.: A multiresolution index of valley bottom flatness for mapping depositional areas, Water Resources Research, 39, https://doi.org/10.1029/2002WR001426, 2003.

Garibaldi, M. C., Bonnaventure, P. P., Noad, N. C., and Kochtitzky, W.: Modelling air, ground surface, and permafrost temperature variability across four dissimilar valleys, Yukon, Canada, Arctic Science, 10, 611–629, https://doi.org/10.1139/as-2023-0067, 2024.

Hersbach, H., Bell, N., Berrisford, P., and et al.: The ERA5 global reanalysis, Quarterly Journal of the Royal Meteorological Society, 146, 1999–2049, https://doi.org/10.1002/qj.3803, 2020.

Hersbach, H., Bell, B., Berrisford, P., Biavati, G., Horányi, A., Muñoz Sabater, J., Nicolas, J., Peubey, C., Radu, R., Rozum, I., Schepers, D., Simmons, A., Soci, C., Dee, D., and Thépaut, J.-N.: ERA5 hourly data on pressure levels from 1940 to present, Copernicus Climate Change Service (C3S) Climate Data Store (CDS), https://doi.org/10.24381/cds.bd0915c6, 2023a.

Hersbach, H., Bell, B., Berrisford, P., Biavati, G., Horányi, A., Muñoz Sabater, J., Nicolas, J., Peubey, C., Radu, R., Rozum, I., Schepers, D., Simmons, A., Soci, C., Dee, D., and Thépaut, J.-N.: ERA5 hourly data on single levels from 1940 to present, Copernicus Climate Change Service (C3S) Climate Data Store (CDS), https://doi.org/10.24381/cds.adbb2d47, 2023b.

Hrebtov, M. and Hanjalić, K.: Numerical Study of Winter Diurnal Convection Over the City of Krasnoyarsk: Effects of Non-freezing River, Undulating Fog and Steam Devils, Boundary-Layer Meteorology, 163, 469–495, https://doi.org/10.1007/s10546-016-0231-0, 2017.

Hughes, J. K., Ross, A. N., Vosper, S. B., Lock, A. P., and Jemmett-Smith, B. C.: Assessment of valley cold pools and clouds in a very high-resolution numerical weather prediction model, Geoscientific Model Development, 8, 3105–3117, https://doi.org/10.5194/gmd-8-3105-2015, 2015.

Kosaka, Y., Kobayashi, S., Harada, Y., Kobayashi, C., Naoe, H., Yoshimoto, K., Harada, M., Goto, N., Chiba, J., Miyaoka, K., Sekiguchi, R., Deushi, M., Kamahoria, H., Nakaegawa, T., Tanaka, T. Y., Tokuhiro, T., Sato, Y., Matsushita, Y., and Onogi, K.: The JRA-3Q Reanalysis, Journal of the Meteorological Society of Japan. Ser. II, 102, 49–109, https://doi.org/10.2151/jmsj.2024-004, 2024.

LaZerte, S. E. and Albers, S.: weathercan: Download and format weather data from Environment and Climate Change Canada, The Journal of Open Source Software, 3, 571, https://doi.org/10.21105/joss.00571, 2018.

https://doi.org/10.5194/egusphere-2025-5512
Preprint. Discussion started: 6 February 2026

Lewkowicz, A. G. and Bonnaventure, P. P.: Equivalent Elevation: A New Method to Incorporate Variable Surface Lapse Rates into Mountain Permafrost Modelling, Permafrost and Periglacial Processes, 22, 153–162, https://doi.org/10.1002/ppp.720, 2011.

Liu, Z., Guo, D., Hua, W., and Chen, Y.: Near-surface permafrost extent and active layer thickness characterized by reanalysis/assimilation data, Atmospheric Science Letters, 26, https://doi.org/10.1002/asl.1289, 2025.

Mayfield, J. A. and Fochesatto, G. J.: The Layered Structure of the Winter Atmospheric Boundary Layer in the Interior of Alaska, Journal of Applied Meteorology and Climatology, 52, 953 – 973, https://doi.org/10.1175/JAMC-D-12-01.1, 2013.

Nkiaka, E., Nawaz, N. R., and Lovett, J. C.: Evaluating Global Reanalysis Datasets as Input for Hydrological Modelling in the Sudano-Sahel Region, Hydrology, 4, https://doi.org/10.3390/hydrology4010013, 2017.

Noad, N. C. and Bonnaventure, P. B.: Spatiotemporal variability of surface-based temperature inversions in high-latitude northcentral Yukon valleys measured utilizing a dense network of elevation transects, manuscript submitted for publication, 2025.

Noad, N. C. and Bonnaventure, P. P.: Surface temperature inversion characteristics in dissimilar valleys, Yukon Canada, Arctic Science, 8, 1320–1339, https://doi.org/10.1139/as-2021-0048, 2022.

Noad, N. C. and Bonnaventure, P. P.: Examining the influence of microclimate conditions on the breakup of surface-based temperature inversions in two proximal but dissimilar Yukon valleys, Canadian Geographies / Géographies canadiennes, 68, 323–339, https://doi.org/10.1111/cag.12886, 2024.

Noad, N. C., Bonnaventure, P. P., Gilson, G. F., Jiskoot, H., and Garibaldi, M. C.: Surface-based temperature inversion characteristics and impact on surface air temperatures in northwestern Canada from radiosonde data between 1990 and 2016, Arctic Science, 9, 545–563, https://doi.org/10.1139/as-2022-0031, 2023.

Noad, N. C., Pozsgay, V., Bonnaventure, P. P., and Gruber, S.: Validation of Point-Scale Climate Reanalysis Models Calibrated for Surface-Based Temperature Inversions Utilizing In-Situ Measures in Northcentral Yukon Valleys, manuscript in preparation, 2025.

Ntagkounakis, G. E., Nastos, P. T., and Kapsomenakis, Y.: Statistical Downscaling of ERA5 Reanalysis Precipitation over the Complex Terrain of Greece, Environmental Sciences Proceedings, 26, https://doi.org/10.3390/environsciproc2023026081, 2023.

Obu, J., Westermann, S., Bartsch, A., Berdnikov, N., Christiansen, H. H., Dashtseren, A., Delaloye, R., Elberling, B., Etzelmüller, B., Kholodov, A., Khomutov, A., Kääb, A., Leibman, M. O., Lewkowicz, A. G., Panda, S. K., Romanovsky, V., Way, R. G., Westergaard-Nielsen, A., Wu, T., Yamkhin, J., and Zou, D.: Northern Hemisphere permafrost map based on TTOP modelling for 2000–2016 at 1 km2 scale, Earth-Science Reviews, 193, 299–316, https://doi.org/10.1016/j.earscirev.2019.04.023, 2019.

Oyler, J. W., Dobrowski, S. Z., Ballantyne, A. P., Klene, A. E., and Running, S. W.: Artificial amplification of warming trends across the mountains of the western United States, Geophysical Research Letters, 42, 153–161, https://doi.org/10.1002/2014GL062803, 2015.

Park, H., Watanabe, E., Kim, Y., Polyakov, I., Oshima, K., Zhang, X., Kimball, J. S., and Yang, D.: Increasing riverine heat influx triggers Arctic sea ice decline and oceanic and atmospheric warming, Science Advances, 6, https://doi.org/10.1126/sciadv.abc4699, 2020.

Pepin, N. C., Arnone, E., Gobiet, A., Haslinger, K., Kotlarski, S., Notarnicola, C., Palazzi, E., Seibert, P., Serafin, S., Schöner, W., Terzago, S., Thornton, J. M., Vuille, M., and Adler, C.: Climate Changes and Their Elevational Patterns in the Mountains of the World, Reviews of Geophysics, 60, https://doi.org/10.1029/2020RG000730, 2022.

Porter, C., Howat, I., Noh, M.-J., Husby, E., Khuvis, S., Danish, E., Tomko, K., Gardiner, J., Negrete, A., Yadav, B., Klassen, J., Kelleher, C., Cloutier, M., Bakker, J., Enos, J., Arnold, G., Bauer, G., and Morin, P.: ArcticDEM - Mosaics, Version 4.1, https://doi.org/10.7910/DVN/3VDC4W, 2023.

https://doi.org/10.5194/egusphere-2025-5512
Preprint. Discussion started: 6 February 2026

Pozsgay, V. and Gruber, S.: Modelling the temporal dynamics of subarctic surface temperature inversions from atmospheric reanalysis for producing point-scale multi-decade meteorological time series in mountains, Arctic Science, 11, 1–16, https://doi.org/10.1139/as-2025-0027, 2025.

Pozsgay, V., Noad, N. C., Bonnaventure, P. P., and Gruber, S.: DReaMIT, https://doi.org/10.5281/zenodo.17545268, 2025.

Prowse, T. D., Bonsal, B. R., Duguay, C. R., and Lacroix, M. P.: River-ice break-up/freeze-up: a review of climatic drivers, historical trends and future predictions, Annals of Glaciology, 46, 443–451, https://doi.org/10.3189/172756407782871431, 2007.

Riseborough, D., Shiklomanov, N., Etzelmüller, B., Gruber, S., and Marchenko, S.: Recent advances in permafrost modelling, Permafrost and Periglacial Processes, 19, 137–156, https://doi.org/10.1002/ppp.615, 2008.

Roberts, D. R., Wood, W. H., and Marshall, S. J.: Assessments of downscaled climate data with a high-resolution weather station network reveal consistent but predictable bias, International Journal of Climatology, 39, 3091–3103, https://doi.org/10.1002/joc.6005, 2019.

Sheridan, P. F.: Synoptic-flow interaction with valley cold-air pools and effects on cold-air pool persistence: Influence of valley size and atmospheric stability, Quarterly Journal of the Royal Meteorological Society, 145, 1636–1659, https://doi.org/10.1002/qj.3517, 2019.

Tao, J., Koster, R. D., Reichle, R. H., Forman, B. A., Xue, Y., Chen, R. H., and Moghaddam, M.: Permafrost variability over the Northern Hemisphere based on the MERRA-2 reanalysis, The Cryosphere, 13, 2087–2110, https://doi.org/10.5194/tc-13-2087-2019, 2019.

Tarek, M., Brissette, F. P., and Arsenault, R.: Evaluation of the ERA5 reanalysis as a potential reference dataset for hydrological modelling over North America, Hydrology and Earth System Sciences, 24, 2527–2544, https://doi.org/10.5194/hess-24-2527-2020, 2020.

Tikhomirov, A. B., Lesins, G., and Drummond, J. R.: Drone measurements of surface-based winter temperature inversions in the High Arctic at Eureka, Atmospheric Measurement Techniques, 14, 7123–7145, https://doi.org/10.5194/amt-14-7123-2021, 2021.

Urban, M., Eberle, J., Hüttich, C., Schmullius, C., and Herold, M.: Comparison of Satellite-Derived Land Surface Temperature and Air Temperature from Meteorological Stations on the Pan-Arctic Scale, Remote Sensing, 5, 2348–2367, https://doi.org/10.3390/rs5052348, 2013.

Urraca, R. and Gobron, N.: Temporal stability of long-term satellite and reanalysis products to monitor snow cover trends, The Cryosphere, 17, 1023–1052, https://doi.org/10.5194/tc-17-1023-2023, 2023.

Wang, T., Hamann, A., Spittlehouse, D., and Carroll, C.: Locally Downscaled and Spatially Customizable Climate Data for Historical and Future Periods for North America, PLOS ONE, 11, 1–17, https://doi.org/10.1371/journal.pone.0156720, 2016.

Way, R. G. and Bonnaventure, P. P.: Testing a reanalysis-based infilling method for areas with sparse discontinuous air temperature data in northeastern Canada, Atmospheric Science Letters, 16, 398–407, https://doi.org/10.1002/asl2.574, 2015.

Zhang, Y., Qian, B., and Hong, G.: A Long-Term, 1-km Resolution Daily Meteorological Dataset for Modeling and Mapping Permafrost in Canada, Atmosphere, 11, https://doi.org/10.3390/atmos11121363, 2020.